Geophysical Journal International

Geophys. J. Int. (2011) **187,** 529–537 doi: 10.1111/j.1365-246X.2011.05170.x

Antipodal focusing of seismic waves due to large meteorite impacts on Earth

Matthias A. Meschede,[1,2,3] Conor L. Myhrvold[1] and Jeroen Tromp[1,4]

[1]*Department of Geosciences, Princeton University, Princeton,* NJ 08544*, USA. E-mail: matthias.meschede@googlemail.com*
[2]*Department of Earth and Environmental Sciences, Ludwig-Maximilians-Universität München, Munich, Germany*
[3]*Department of Physics, Ludwig-Maximilians-Universität München, Munich, Germany*
[4]*Princeton University, Program in Applied & Computational Mathematics, Princeton,* NJ 08544*, USA*

Accepted 2011 July 22. Received 2011 July 9; in original form 2011 March 11

SUMMARY

We examine focusing of seismic waves at the antipode of large terrestrial meteorite impacts, using the Chicxulub impact as our case study. Numerical simulations are based on a spectral-element method, representing the impact as a Gaussian force in time and space. Simulating the impact as a point source at the surface of a spherically symmetric earth model results in deceptively large peak displacements at the antipode. Earth's ellipticity, lateral heterogeneity and a spatially distributed source limit high-frequency waves from constructively interfering at the antipode, thereby reducing peak displacement by a factor of 4. Nevertheless, for plausible impact parameters, we observe peak antipodal displacements of ∼4 m, dynamic stresses in excess of 15 bar, and strains of 2×10^{-5}. Although these values are significantly lower than prior estimates, mainly based on a point source in a spherically symmetric earth model, wave interference en route to the antipode induces 'channels' of peak stress that are five times greater than in surrounding areas. Underneath the antipode, we observed 'chimneys' of peak stress, strain and velocity, with peak values exceeding 50 bar, 10^{-5} and 0.1 m s^{-1}, respectively. Our results put quantitative constraints on the feasibility of impact-induced antipodal volcanism and seismicity, as well as mantle plume and hotspot formation.

Key words: Guided waves; Computational seismology; Wave propagation; Impact phenomena; Large igneous provinces; Planetary volcanism.

1 INTRODUCTION

Ground motion induced by a major meteorite impact on Earth can lead to peak displacements exceeding those produced by even the largest earthquakes (Toon *et al.* 1997; Collins *et al.* 2005). An initial supersonic shock wave generated by the impact decays into strong compressional body waves, and powerful Rayleigh surface waves are emitted in all azimuths. At shallow impact angles, strong shear body waves and Love surface waves are also produced.

Since Earth is nearly spherical it acts as a lens, focusing seismic waves on the opposite side of the globe, the antipode. Body waves, which travel through the interior, are focused by reflection and refraction. Surface waves, the main carriers of seismic energy, propagate circularly away from the impact location along Earth's surface and converge at the antipode.

Both artificial impacts in laboratory environments (Gault & Wedekind 1969) and theoretical studies suggest that antipodal focusing results in severely increased displacements, leading to a notable aftermath at the opposite side of a planet or moon (Schultz & Gault 1974; Hughes *et al.* 1977). Furthermore, predictions of antipodal disruptions lead to structural constraints on planetary interiors (Watts *et al.* 1991; Bruesch & Asphaug 2004). Planetary-scale impacts may even produce antipodal crustal removal and melting (Marinova *et al.* 2008, 2011; Nimmo *et al.* 2008).

So far, studies have employed spherically symmetric planetary models, neglecting influences of ellipticity, lateral heterogeneity or oblique impact. For example, antipodal focusing after the Chicxulub impact, widely believed to be responsible for the 65 Ma mass extinction event, has been modelled using normal-mode summation for a spherically symmetric earth model (Boslough *et al.* 1996; Ni & Ahrens 2006). Previous studies have linked focusing effects to triggering of antipodal volcanism and seismicity, and the creation of mantle plumes and hotspots, which seem to frequently occur in antipodal pairs (Rampino & Caldeira 1992). In the case of Chicxulub, antipodal triggering effects are particularly interesting in connection to the K–T mass extinction.

In this study, we use the spectral-element solver SPECFEM3D_GLOBE (Komatitsch & Tromp 2002a,b) to simulate global seismic wave propagation induced by a Chicxulub-scale impact. The spectral-element mesh honours Earth's ellipticity, topography, bathymetry and crustal thickness variations. Wave speeds and densities are determined by mantle model S362ANI

(Kustowski *et al.* 2008) in combination with crustal model CRUST2.0 (Bassin *et al.* 2000). The simulations accommodate rotation, self-gravitation and attenuation.

In the first instance, the source is modelled as a point force oriented in the impact direction with a Gaussian source–time function, using Chicxulub-scale impact parameters. In addition, we compare the effects of a finite source distributed approximately over the crater region with those of a point source. The duration of the impact is controlled by the width of the Gaussian source–time function. Finally, we examine effects of oblique impacts, and provide quantitative estimates for peak displacements, velocities, stresses and strains at the antipode and throughout the mantle.

2 IMPACT MODEL

Just as earthquakes may be represented by an equivalent centroid-moment tensor (effectively a double-couple point source), thereby capturing global long-period ground motions, an impact may be represented by an equivalent single-force point source. Such a representation is, of course, invalid in the impact's inelastic vicinity—approximately one crater width (Ahrens & O'Keefe 1977; Melosh 1989)—but accurately captures the long-period seismic wavefield elsewhere. Short-period waves, which are not accurately represented by our simplified source spectrum, become more important for peak quantities as we approach the source. The appendix provides a qualitative comparison with a detailed impact source calculation by Ivanov (2005).

2.1 Point force

We model the impact of a stone bolide with a 10 km diameter as a point force, using a momentum of $\Delta p = 3 \times 10^{19}$ N s, following prior work by Boslough *et al.* (1996), and additional parameters summarized in Table 1. This momentum is transmitted by the force per unit volume

$$\boldsymbol{f}(\boldsymbol{x}, t) = \hat{\boldsymbol{f}}\, F\, S(t)\, \delta(\boldsymbol{x} - \boldsymbol{x}_s) \tag{1}$$

with amplitude $F = 3 \times 10^{19}$ N, normalized impact direction $\hat{\boldsymbol{f}}$, impact location $\boldsymbol{x}_s$ and normalized time- and frequency-domain Gaussian source–time functions

$$S(t) = \sqrt{\frac{\pi}{\tau^2}}\, \exp\left(-\pi^2 t^2/\tau^2\right), \tag{2}$$

$$S(f) = \exp\left(-f^2\tau^2\right). \tag{3}$$

The parameter τ denotes the period below which the amplitude of the radiated waves is decreased to $1/e$ (the e-folding time). This parameter is important for determining the necessary mesh resolution and therefore the frequency resolution of the solver. The parameter τ also describes the width of the source–time function, which is connected to the dissipating shock wave after the impact. Its exact value remains unknown, but we show that its influence across the range of impact-appropriate values is limited. We therefore approximate its value by scaling the kinetic energy of the impactor (see Section 2.3), realizing that the uncertainty associated with determining τ is dwarfed by other uncertainties. We model oblique impacts with a westward (270°) directed force at a 45° angle to the surface. Since Chicxulub's impact direction and obliqueness are controversial and difficult to obtain from the shape of a crater (Elbeshausen *et al.* 2009), these values are arbitrary but plausible.

Table 1. Chicxulub-scale impact parameters.

Diameter	10 km
Density	2.7 g cm^{-3}
Velocity	20 km s^{-1}
Momentum	$\sim 3 \times 10^{19}$ N s
Kinetic energy	$\sim 3 \times 10^{23}$ J

2.2 Earth model

Our earth model combines 3-D mantle model S362ANI (Kustowski *et al.* 2008) with crustal model CRUST2.0 (Bassin *et al.* 2000). We incorporate the solid inner core, fluid outer core, ellipticity, topography and bathymetry, the oceans, rotation and self-gravitation using the spectral-element solver SPECFEM3D_GLOBE. Our spectral-element mesh accurately resolves waves with periods of 17 s and greater. The grid is designed to maintain at least five gridpoints per minimum wavelength and satisfies the Courant stability condition, as governed by the compressional and shear wave speeds. At the surface, it reaches an average node spacing of 10 km. Details about the implementation and mesh may be found in Komatitsch & Tromp (2002a,b). For spherically symmetric reference simulations, we use transversely isotropic model PREM (Dziewonski & Anderson 1981), including effects of attenuation and self-gravitation.

Since our 3-D model is based on today's Earth's structure, the impact location and corresponding antipode location are inaccurate with respect to past continent configurations. The impact location was chosen to mimic Chicxulub's impact location with respect to the Eurasian and American landmasses, which were closer together 65 Ma. The chosen position therefore deviates from the present-day crater position in the Yucatan and lies in the Atlantic Ocean (25°N, 63°W). The ancient antipode position was north of Australia and not on the continent, as in our simulations. We therefore merely use the simulations to demonstrate the effects of today's heterogeneities, which should be comparable to the influence of ancient Earth's structure.

2.3 Source energy

In solving the momentum equation, we do not explicitly specify source energy in spectral-element simulations. To estimate its value, we approximate the source energy analytically for a point force in a homogeneous medium, following Madariaga (2007):

$$E_P = \frac{F^2}{12\pi\rho\,\alpha^3} \int_{-\infty}^{\infty} \dot{S}^2(t)\, \mathrm{d}t, \tag{4}$$

$$E_S = \frac{F^2}{6\pi\rho\,\beta^3} \int_{-\infty}^{\infty} \dot{S}^2(t)\, \mathrm{d}t, \tag{5}$$

$$E_{\mathrm{seis}}(\tau) = \frac{F^2\pi^{3/2}}{2^{5/2}\,\tau^3\,\rho} \left(\frac{1}{3\alpha^3} + \frac{2}{3\beta^3}\right), \tag{6}$$

where E_P, E_S and E_{seis} denote the P-wave, S-wave and total seismic energy, respectively, and the source–time function is defined by (2). The parameters ρ, α and β denote density, compressional and shear wave speeds, respectively, which we choose as in a crustal environment. Decreasing the parameter τ therefore increases the radiated energy (as also stipulated by eq. 3).

Since we solve a momentum conservation equation—the linear seismic wave equation as in Komatitsch & Tromp (2002a,b)—we fix the total transferred momentum, as the integral of force over

time, to the momentum of the meteorite (parameter F in eq. 1). The total seismic energy as a fraction of the impact energy, or seismic efficiency, depends on the particular form of momentum transmission, specified by $S(t)$. Seismic efficiency of a large impact is not well constrained, but may be estimated from results of laboratory-scale impact experiments, missile impacts and explosions, as well as from theoretical arguments.

Values from Schultz & Gault (1974) suggest that the seismic efficiency factor k, which is defined by $E_{\rm seis} = k \times E_{\rm kin}$, is around $k = 10^{-4}$ (where $E_{\rm kin}$ denotes the kinetic energy of the impactor). However, they also report efficiency factors of 10^{-5} and 10^{-6}, and even suggest it may be larger than 10^{-4} for large, deeply penetrating impacts. A newer theoretical study by Shishkin (2007), however, finds a decreasing dependency of seismic efficiency on impactor size as well as velocity, and suggests values between 10^{-4} and 10^{-5} for our scenario. In comparison, Shishkin (2007) proposes up to $k \sim 10^{-2}$ for slower, smaller impactors (100 m diameter, 12 km s^{-1} velocity), and $k \sim 10^{-1}$ for buried explosions.

The kinetic energy of the Chicxulub impact is on the order of $E_{\rm kin} \sim 3 \times 10^{23}$ J. We may use a source–time function with τ between ∼20 s ($k \sim 4 \times 10^{-3}$) and ∼200 s ($k \sim 3 \times 10^{-6}$) to produce energies of 10^{18}–10^{20} J, appropriate for a range of seismic efficiencies. We use a default value of $\tau = 58$ s, which corresponds in a crustal environment to an energy of $E_{\rm seis} = 4 \times 10^{19}$ J and $k \sim 10^{-4}$ (see Fig. 1). To demonstrate the influence of a higher seismic efficiency, we use $\tau = 19$ s, which corresponds to $k \sim 4 \times 10^{-3}$.

Note that the equations we solve scale linearly with momentum but not with energy. Keeping τ constant, twice the momentum simply leads to twice the displacement. Keeping the momentum constant, twice the energy decreases τ, thereby amplifying high-frequency displacements while leaving low-frequency amplitudes basically unchanged (see eq. 3). Of course, momentum and τ, or seismic efficiency k, cannot be seen as two independent variables. Following Shishkin (2007), increasing mass or velocity—and thus momentum—decreases the seismic efficiency and increases τ. Apart from the seismic efficiency argument, it seems plausible to assume a larger impact to have a wider source–time function, generating a broader, longer lasting pulse. A direct calculation of τ from impact parameters should be feasible, but would require detailed modelling of the impact process.

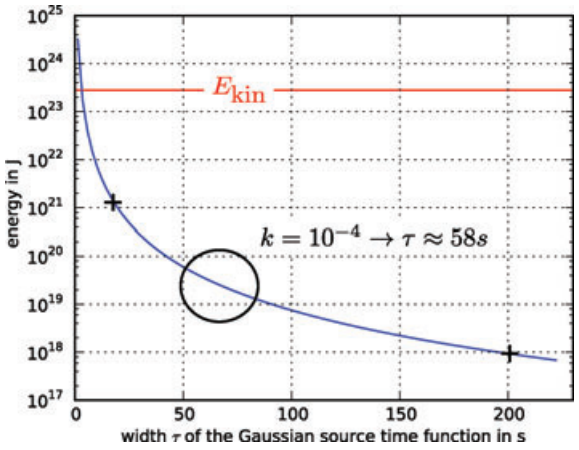

Figure 1. Seismic energy $E_{\rm seis}$, given by eq. (6), radiated by a point force in a homogeneous medium. A seismic efficiency of $k = 10^{-4}$, roughly denoted by the black circle, leads to a Gaussian source–time function with a value of $\tau = 58$ s. The two black crosses show the approximate upper and lower limits for plausible k, τ combinations. The kinetic energy of the bolide, $E_{\rm kin}$, is indicated by the red horizontal line.

For antipodal peak displacements, short-period waves play a less significant role, since on their way to the antipode they are more strongly influenced by lateral heterogeneity and are less likely to interfere constructively due to their short wavelengths.Therefore, linear scaling with momentum still holds for antipodal peak displacements, since constructive interference of lower frequency waves is less sensitive to τ. Nevertheless, higher frequency waves do affect antipodal peak stresses, as illustrated in Section 3.5. Away from the antipode, peak displacements scale increasingly less than linear with momentum, since, together with the efficiency, the high-frequency content is reduced.

3 RESULTS

3.1 Influence of the source spectrum

In our model, the impact spectrum is determined by the Gaussian source–time function (2), which limits high frequencies. Unfortunately, the precise parameter value of τ for the Chicxulub impact is uncertain. Shorter durations produce higher frequency waves, which should affect resulting peak amplitudes. Fig. 2 shows peak antipodal displacements after a vertical impact for various values of τ . Decreasing τ leads to higher peak displacements in the spherically symmetric model, where waves with arbitrary frequencies all constructively interfere. However, peak antipodal displacements in the 3-D model are relatively unaffected by high frequencies.

Since short-period waves are more significantly influenced by lateral heterogeneity than long-period waves, the main contribution to peak antipodal displacements comes from the constructive interference of low frequencies. A finite source has a similar effect, which we model by distributing the force over a larger surface area using a Gaussian with an e-folding distance of approximately 100 km (resembling a crater with a diameter of ∼200 km). This distributed source reduces peak antipodal displacements, as illustrated in Fig. 2.

Stress and other higher order parameters (i.e. parameters involving differentiation of the displacement) can increase dramatically with a higher frequency source spectrum. For such parameters, we explicitly model a higher seismic efficiency to assess their sensitivity to τ.

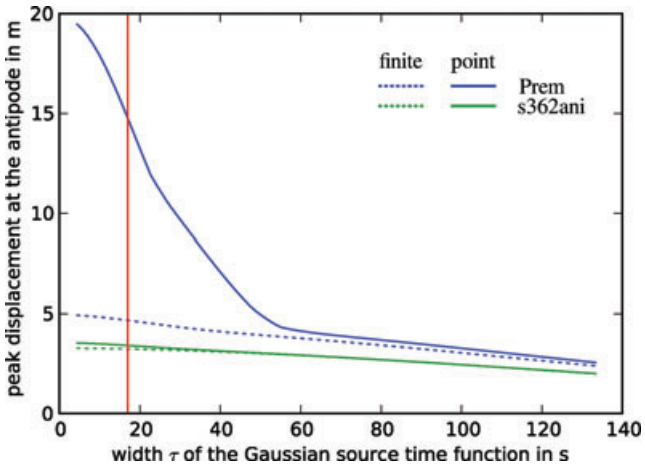

Figure 2. Peak antipodal displacements in spherically symmetric model PREM (blue solid and dashed lines) and 3-D model S362ANI+CRUST2.0 (green solid and dashed lines). Dashed lines correspond to a point source, solid lines to a finite source. The red vertical line shows the mesh resolution limit of ∼17 s.

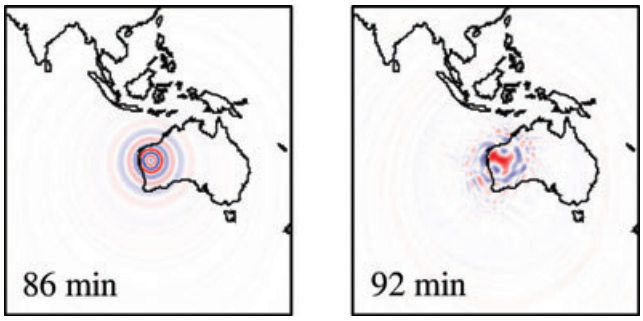

Figure 3. Close-up of the antipodal vertical velocity wavefield after a Chicxulub-scale impact for spherically symmetric model PREM (left-hand side) and 3-D model S362ANI+CRUST2.0 (right-hand side) using a vertical impact direction. Note that contours of the continents are today's, not their end Cretaceous positions, and therefore do not show the original Chicxulub antipode 65 Ma.

3.2 Time evolution of the wavefield

The influence of lateral heterogeneity on antipodal focusing can be seen in a snapshot of the vertical velocity wavefield on the surface due to a vertical impact, as shown in Fig. 3 . On the left-hand side, we use spherically symmetric earth model PREM. On the right-hand side, we use 3-D mantle model S362ANI in combination with crustal model CRUST2.0. The strong blue and red waves are Rayleigh waves which are just converging on the antipode. The effects of lateral heterogeneity are clearly evident by comparing the two snapshots. In the symmetric model, surface waves are expected to constructively interfere at a single point due to their identical great-circle path lengths, leading to dramatic peak antipodal displacements well in excess of 10 m, confirming prior estimates (see the appendix for a quantitative comparison between our spherically symmetric calculations and prior work by Boslough *et al.* 1996).

In the 3-D earth model, path lengths and antipodal traveltimes differ, and Rayleigh waves do not necessarily constructively interfere at the antipode. This reduced constructive interference leads to reduced antipodal displacements. In contrast to a spherically symmetric model, where surface wave rays intersect exactly at the antipode, a 3-D model produces complicated antipodal surface wave caustics.

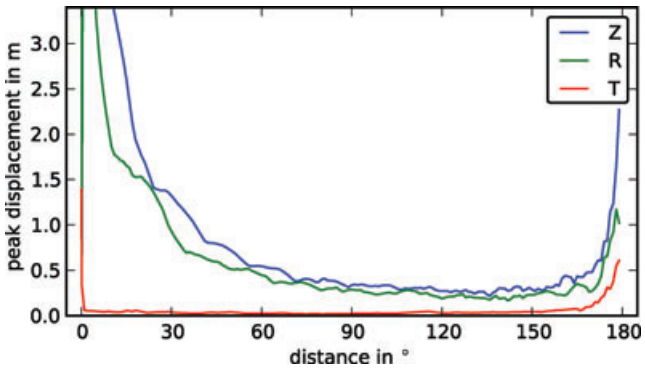

Figure 5. Peak vertical (Z), radial (R) and transverse (T) displacements along a great circle for a vertical impact in 3-D model S362ANI+CRUST2.0.

3.3 Peak amplitudes

Peak displacement values may be visualized in terms of isosurfaces to demonstrate their 3-D distribution. Since the largest displacements occur near the surface, due to the strong surface waves, the isosurfaces create cap-like structures directly beneath the surface. Fig. 4 compares peak displacement isosurfaces in the impact and antipodal hemispheres. Fig. 5 illustrates peak vertical, radial and transverse displacements along an arbitrary great circle through the impact point, for the vertical impact case, illustrating the negligible generation of transversely polarized Love surface waves.

In the impact hemisphere, the influence of strong lateral heterogeneity leads to the rugged structure of the isosurface caps. The thick slow crust of the Andes, for example, bends waves towards them, increasing peak amplitudes, as in a waveguide. Such effects lead to an antipodal focusing structure with a star- rather than a point-like shape. The topology of antipodal caustics was ray-theoretically simulated by Wang *et al.* (1993). At the antipode, peak displacements reach values of ∼4 m.

In the 3-D model, interference of surface waves on their way to the antipode leads to channel-like structures (see Blitz 2009, for similar simulations of such channels on the asteroid Eros). Fig. 6 shows the peak norm of the stress tensor, $||\mathbf{T}|| = \frac{1}{\sqrt{2}}(\mathbf{T} : \mathbf{T})^{1/2}$, at a depth of 60 km. Peak stress decreases rapidly towards the surface because the traction vanishes at the free surface. Due to caustics,

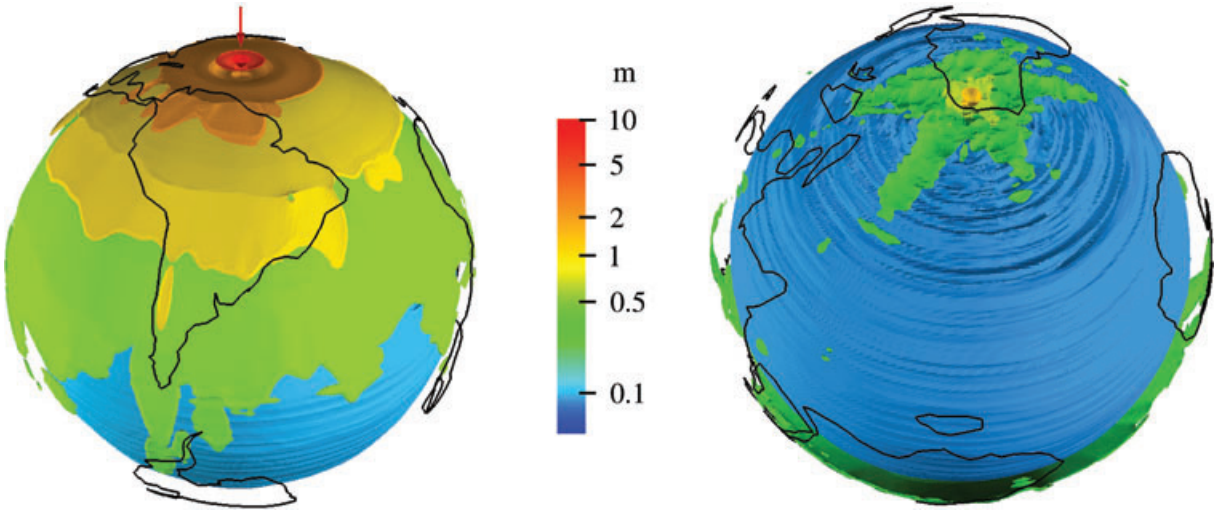

Figure 4. Isosurfaces of the norm of the peak displacement vector after a vertical impact for the impact hemisphere (left-hand side) and antipodal hemisphere (right-hand side).

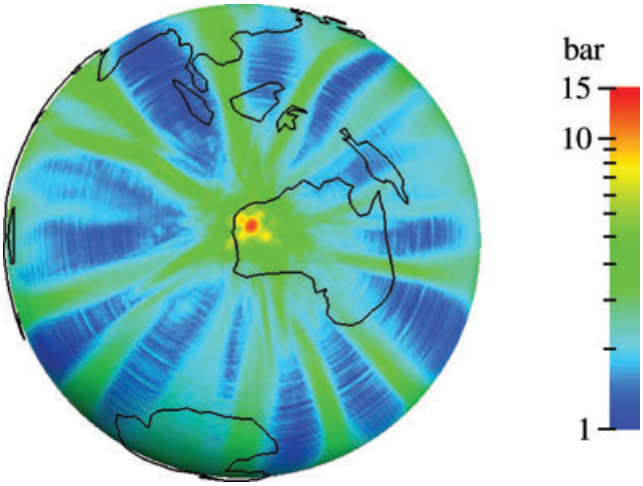

Figure 6. Peak of the norm of the stress tensor at 60 km depth in the antipodal hemisphere for a vertical impact. Note the 4–5 bar stress 'channels' associated with focusing of the Rayleigh surface wavefield.

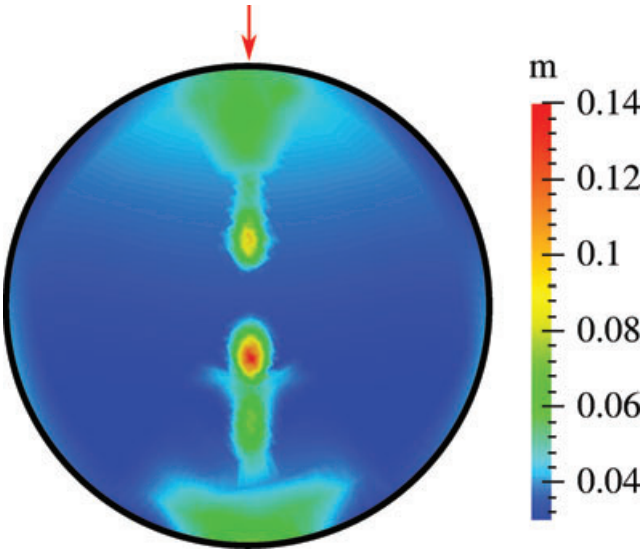

Figure 7. Norm of peak inner core displacement vector. Focusing of compressional body waves induces displacements in excess of 10 cm in the inner core. The impact direction is shown by the red arrow. The two focusing spots reflect the predominantly ellipsoidal shape of the Earth.

peak channels of stress—seen as green stripes in Fig. 6—involve five times larger stresses than in surrounding areas. In the antipodal hemisphere and near the surface, peak stresses are 1–5 bar and approach 15 bar at the antipode. A simulation with a value of $\tau =$ 19 s and a 40 times higher seismic efficiency increases peak stresses at 60 km depth by a factor of ∼3 (figure not shown).

Peak displacements inside the inner core show two focusing regions slightly offset from Earth's centre, as shown in Fig. 7 . This is a consequence of Earth's predominantly ellipsoidal shape: in a spherically symmetric earth model the waves would focus at the centre. Inner core peak displacements reach more than 10 cm.

3.4 Angle of impact

Fig. 8 illustrates the effect of impact angle on peak displacements. The two cross-sections indicate that an oblique impact direction results in more evenly distributed peak displacements throughout the mantle. The shear wave, radiating in a direction perpendicular to the impact direction, clearly contributes significantly to the peak displacement. Focusing occurs in both cases along the impact-antipode axis.

3.5 Peak amplitudes at the antipode

Of special interest is the region beneath the antipode, since here we expect the highest amplitudes of stress and strain away from the impact site, which, it has been proposed, could lead to fracturing of rocks, melting and triggering of secondary phenomena, such as earthquakes or volcanism. Fig. 9 shows cross-sections of peak stress, strain and velocity through the mantle beneath the antipode for vertical and oblique impacts.

As expected, the highest stresses occur along 'chimneys' connecting source and antipode. Focusing is always along this axis, irrespective of impact angle, but the pattern of amplification and deamplification is influenced by the direction and angle of impact. For a 45° impact, high peak stresses (10–15 bar) are observed in the mantle in the depth range ∼1200–1600 km. For a vertical impact, focusing is distributed more evenly along the axis, with peak values of 7.5–10 bar. In both cases, the highest stresses (10–15 bar) occur at the base of the crust, although the vertical impact has a larger focus spot with slightly higher stresses than the 45° case. An increased seismic efficiency ($\tau = 19$ s), however, dramatically increases peak stress mainly inside the mantle by a factor of almost 10, approaching 100 bar.

Compared to stress, seismic efficiency has only a minor influence on the peak values of strain and velocity, increasing them by a factor of ∼2. For the default efficiency, strains are on the order of 2×10^{-5}, with velocities of 0.2 m s^{-1}.

The displacement is also relatively unaffected by the choice of τ. Higher frequencies do slightly increase peak displacements at the surface, but, more importantly, they increase the size of the region of high-amplitude displacement surrounding the antipode (Fig. 10).

4 DISCUSSION

Our simulations demonstrate that several far-field geological consequences are to be expected after a Chicxulub-scale impact, as follows.

(i) Triggering of seismicity. Peak stresses are comparable to observed stress drops in moderate to large seismic events (Allmann & Shearer 2009), making triggering plausible. Triggered events have been reported for peak amplitudes exceeding a few microstrains (Gomberg & Johnson 2005), which we surpass by an order of magnitude. Moreover, a strong correlation has been found in laboratory experiments between faulting and stress loading, occurring for periodic shear stresses above 3 bar (Lockner & Beeler 1999). According to this value, distinctly higher triggering rates would occur inside previously mentioned channels of high stress.

(ii) Triggering of volcanism. Manga & Brodsky (2006) show a correlation between seismicity and volcanism, and point out the significance of dynamic stresses due to far-field seismic waves. At the antipode, we exceed typical stresses associated with triggering (1 − 10 bar) by an order of magnitude. Even so, since multiple triggering mechanisms could be involved, the dependence of triggering rate on stress amplitude and period is not obvious.

(iii) Fracturing of rock. The ultimate strength required to fracture common rocks at atmospheric pressure and room temperature ranges from tens to hundreds (tension) to thousands (compression)

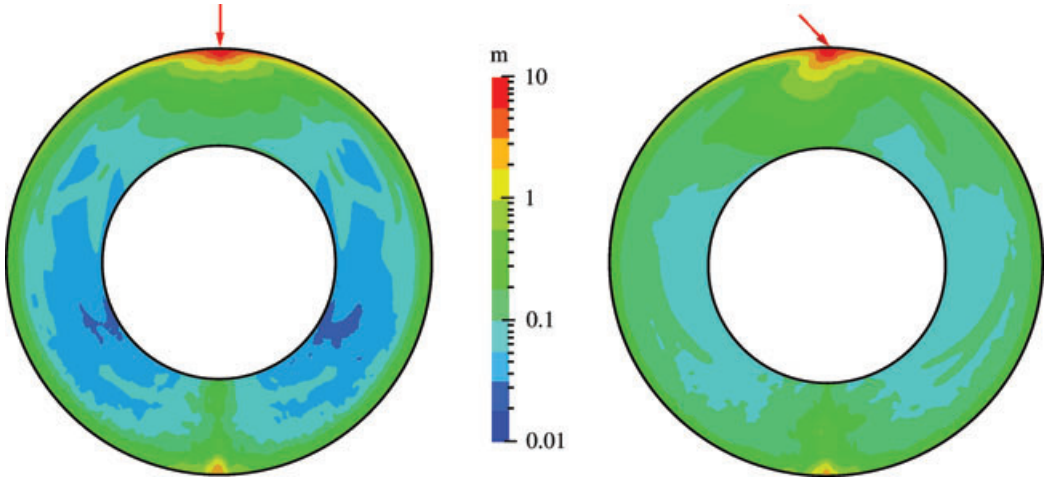

Figure 8. Norm of peak displacement throughout the mantle for a vertical impact (left) and a 45° impact (right).

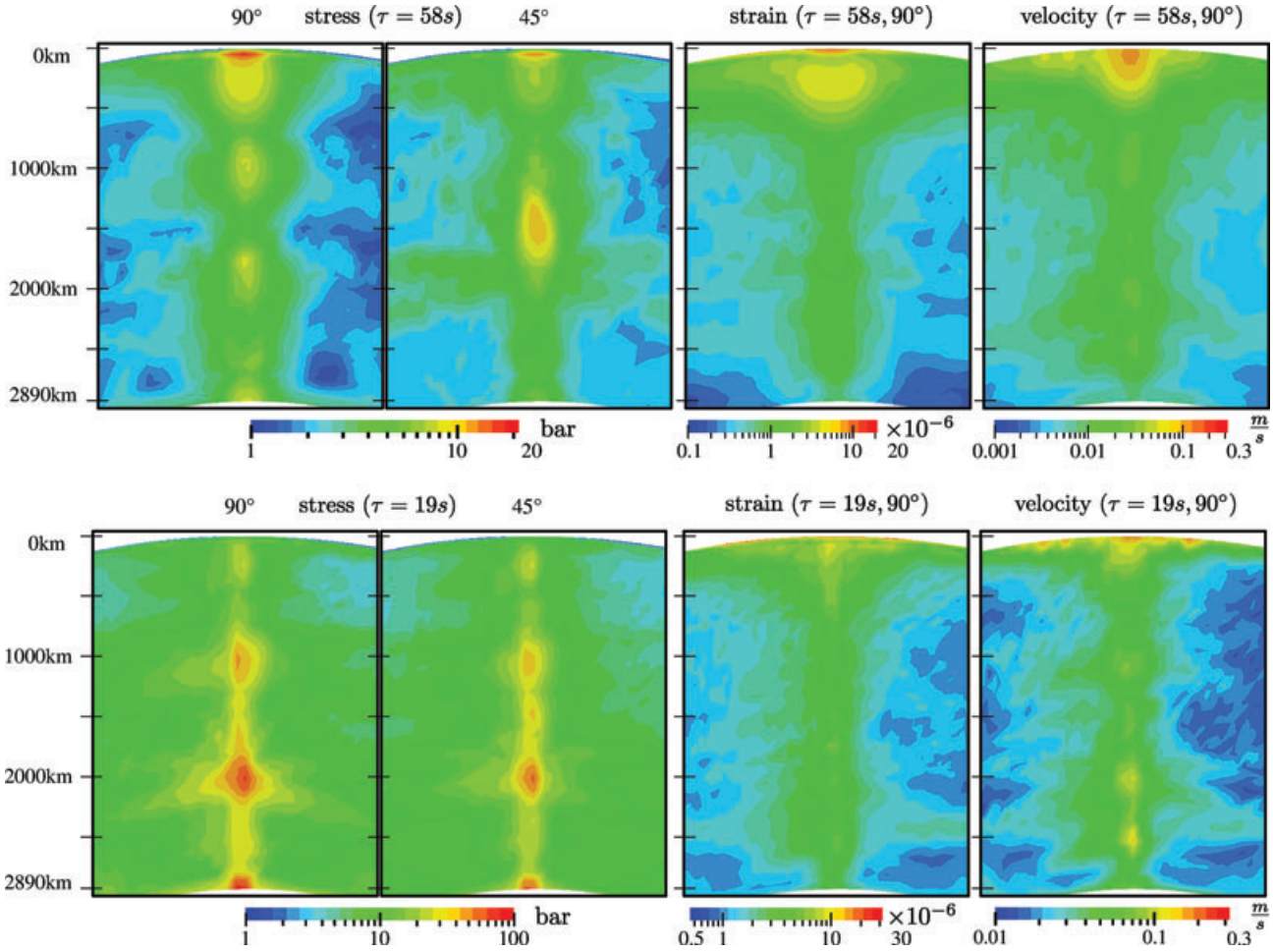

Figure 9. Close-up views of 'chimneys' of peak stress, strain and velocity in a cut-away through the mantle. For peak stress, we consider vertical (column one) and oblique (column two) impact directions, whereas for peak strain (column three) and velocity (column four) we consider a vertical impact. The values of the source parameter τ and seismic efficiency k are $\tau = 58$ s, $k = 10^{-4}$ (top row) and $\tau = 19$ s, $k = 4 \times 10^{-3}$ (bottom row).

of bar (Kim & Lade, 1984). Under confining pressure, deeper in the crust, these values can significantly increase (Handin & Hager 1957). Increased temperatures, on the other hand, weaken rocks (Handin *et al.* 1967). While the latter effect dominates in deeper parts of the crust, in shallow regions the former effect is more important (Kearey *et al.* 2009). At the antipode, our simulations exhibit peak stresses close to those required to fracture weak rocks under surface conditions. Nevertheless, because of the complexity of the mechanisms involved, and because we are at the cusp of the breaking strength, we cannot draw a final conclusion whether fracturing will or will not occur at the antipode.

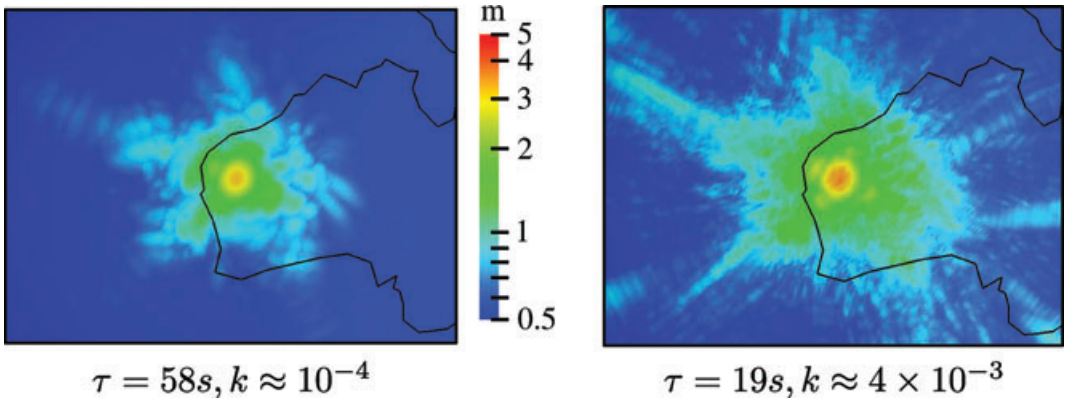

Figure 10. Peak norm of antipodal displacement for a vertical impact with lower (left-hand side) and higher (right-hand side) seismic efficiency k and frequency content τ.

(iv) Melting. Impact-induced antipodal melting has been linked to creation of antipodal hotspot pairs (Rampino & Caldeira 1992), but the energy required for direct melting of corresponding basaltic volumes by dissipation of seismic waves was shown to be orders of magnitude higher than what is to be expected from antipodal seismic dissipation (Melosh 2000). However, as in the case of triggering seismicity and volcanism, the whole anomaly does not have to be created completely by the impact. Discussion about mechanisms is still ongoing (Hagstrum 2005), but a concise quantitative treatment is lacking.

(v) Tsunamis. Apart from a tsunami created directly by an oceanic impact, the antipodal seismic wavefield can also generate a tsunami, even after a continental impact. Our simulations produce oscillatory antipodal displacements with an amplitude of several metres over a large surface area (∼500 km × 500 km), potentially exciting tsunami waves with similar periods of 100 s and greater (Ward 2002). Dawson & Stewart (2007) claim an initial water displacement of at least a metre is required to produce recognizable tsunami-generated deposits, which may be identifiable in the geological record.

5 CONCLUSIONS

We have demonstrated that Earth's lateral heterogeneity and ellipticity and a finite crater size dramatically reduce the influence of high frequency waves on peak antipodal displacements. Compared to peak antipodal displacements of 15 m in a spherically symmetric model, we observe peak displacements of ∼4 m in a more realistic 3-D earth model, mainly determined by constructive long-period waves.

En route to the antipode, the highest wave amplitudes occur along 'channels', where stresses are five times greater than in the immediate surrounding areas and displacements are approximately doubled in magnitude. These channels reflect focusing and defocusing of seismic surface waves, and their width is influenced by Earth's heterogeneous structure and the spectrum of the waves. In addition to surface channeling, significant antipodal focusing occurs in the mantle, creating 'chimneys' of stress, strain and velocity. An oblique impact does not greatly affect peak surface displacements at the antipode, but does influence the distribution of focusing along mantle chimneys.

Our simulations provide an accurate estimate of seismic effects associated with a Chicxulub-scale impact. The effects of any comparable or smaller scale impact may be modelled using the same approach. Modeling a giant, planetary-scale impact requires a nonlinear approach, for example, based on smoothed particle hydrodynamics (Marinova *et al.* 2008, 2011).

Detailed source models based on impact simulations (e.g. Ivanov 2005) could further increase the accuracy of our simulations in regions closer to the source, for example, by using such impact simulations as initial conditions for our simulations at sufficiently large distances from the impact location. Finally, impacts are a convenient seismic source on other planets and our results show how simulations of seismic wave propagation can reveal information about a planet's heterogeneous structure.

ACKNOWLEDGMENTS

Princeton undergraduate Evan Welch helped with the point-force normal-mode simulations. We sincerely thank Garreth Collins for his excellent and comprehensive review, and Shravan Hanasoge, Nathan Myhrvold, Lowell Wood and Daniel Peter for useful feedback and advice. We also thank Heiner Igel and Stuart Gilder for providing financial support. The numerical simulations used in this study were performed on a Dell cluster built and maintained by the Princeton Institute for Computational Science & Engineering. The spectral-element simulations are based on software package SPECFEM3D_GLOBE, which is freely available via the Computational Infrastructure for Geodynamics (geodynamics.org). This research was supported by the National Science Foundation under grant EAR-0711177 and by the German Academic Exchange Service.

REFERENCES

Ahrens, T.J. & O'Keefe, J., 1977. Equations of state and impact-induced shock-wave attenuation on the moon, in *Impact and Explosion Cratering,* pp. 639–656, Pergamon Press, New York, NY.

Allmann, B.P. & Shearer, P.M., 2009. Global variations of stress drop for moderate to large earthquakes, *J. geophys. Res.,* **114,** B01310, doi:10.1029/2008JB005821.

Bassin, C., Laske, G. & Masters, G., 2000. The current limits of resolution for surface wave tomography in North America, *EOS, Trans. Am. geophys. Un.,* **81,** F897.

Blitz, C., 2009. Modélisation de la propagation des ondes sismiques et des ejecta dans les astéroïdes: application á l'érosion des cratéres de l'astéroïde (433) Eros, *PhD thesis,* Institut de Physique du Globe de Paris, 153 pp.

Boslough, M.B., Chael, E.P., Trucano, T.G., Crawford, D.A. & Campbell, D.L., 1996. Axial focusing of impact energy in the Earth's interior: a possible link to flood basalts and hotspots, *Geol. Soc. Am. Spec. Pap.,* **307,** 817–840.

Bruesch, L.S. & Asphaug, E., 2004. Modeling global impact effects on middle-sized icy bodies: applications to Saturn's moons, *Icarus,* **168,** 457–466.

Collins, G.S., Melosh, H.J. & Marcus, R.A., 2005. Earth Impact Effects Program: a web-based computer program for calculating the regional environmental consequences of a meteoroid impact on Earth, *Meteorit. Planet. Sci.,* **40,** 841–864.

Dawson, A. & Stewart, I., 2007. Tsunami deposits in the geological record, *Sediment. Geol.,* **200**(3–4), 166–183.

Dziewonski, A.M. & Anderson, D.L., 1981. Preliminary reference Earth model, *Phys. Earth planet. Inter.,* **25,** 297–356.

Elbeshausen, D., Wnnemann, K. & Collins, G.S., 2009. Scaling of oblique impacts in frictional targets: implications for crater size and formation mechanisms, *Icarus,* **204**(2), 716–731.

Gault, D.E. & Wedekind, J.A., 1969. The destruction of tektites by micrometeoroid impact, *J. geophys. Res.,* **74,** 27, 6780–6794.

Gilbert, F. & Dziewonski, A.M., 1975. An application of normal mode theory to the retrieval of structural parameters and source mechanisms from seismic spectra, *Phil. Trans. R. Soc. Lond., A,* **278,** 1280, 187–269.

Gomberg, J. & Johnson, P., 2005. Dynamic triggering of earthquakes, *Nature,* **437,** 7060, 830.

Hagstrum, J.T., 2005. Antipodal hotspots and bipolar catastrophes: were oceanic large-body impacts the cause? *Earth planet. Sci. Lett.,* **236**(1–2), 13–27.

Handin, J. & Hager, R.V., Jr., 1957. Experimental deformation of sedimentary rocks under confining pressure: tests at room temperature on dry samples, *Am. Assoc. Petrol. Geol. Bull.,* **41,** 1, 1–50.

Handin, J., Heard, H.C. & Magouirk, J.N., 1967. Effects of the intermediate principal stress on the failure of limestone, dolomite, and glass at different temperatures and strain rates, *J. geophys. Res.,* **72**(2), 611–640.

Hughes, H.G., App, F.N. & McGetchin, T.R., 1977. Global seismic effects of basin-forming impacts, *Phys. Earth planet. Inter.,* **15**(2–3), 251–263.

Ivanov, B., 2005. Numerical modeling of the largest terrestrial meteorite craters, *Sol. Syst. Res.,* **39,** 5, 381–409.

Kearey, P., Klepeis, K.A. & Vine, F.J., 2009. *Global Tectonics,* 3rd edn, Wiley-Blackwell, Oxford, ISBN 978-1-4051-0777-8.

Kim, M.K. & Lade, P.V., 1984. Modelling rock strength in three dimensions, *Int. J. Rock Mech. Min. Sci. Geomech. Abstr.,* **21**(1), 21–33.

Komatitsch, D. & Tromp, J., 2002a. Spectral-element simulations of global seismic wave propagation—I. Validation, *Geophys. J. Int.,* **149,** 2, 390–412.

Komatitsch, D. & Tromp, J., 2002b. Spectral-element simulations of global seismic wave propagation—II. 3-D models, oceans, rotation, and self-gravitation, *Geophys. J. Int.,* **150,** 1, 303–318.

Kustowski, B., Dziewonski, A.M. & Ekstrom, G., 2008. Anisotropic shear-wave velocity structure of the Earth's mantle: a global model, *J. geophys. Res.,* **113,** B06306, doi:10.1029/2007JB005169.

Lockner, D.A. & Beeler, N.M., 1999. Premonitory slip and tidal triggering of earthquakes, *J. geophys. Res.,* **104,** B9, doi:10.1029/1999JB900205.

Madariaga, R., 2007. Seismic source theory, *Treatise on Geophysics,* **4,** 60–63.

Manga, M. & Brodsky, E., 2006. Seismic triggering of eruptions: volcanoes and geysers, *Annu. Rev. Earth planet. Sci.,* **34,** 263–291.

Marinova, M.M., Aharonson, O. & Asphaug, E., 2008. Mega-impact formation of the Mars hemispheric dichotomy, *Nature,* **453,** 1216–1219.

Marinova, M.M., Aharonson, O. & Asphaug, E., 2011. Geophysical consequences of planetary-scale impacts into a Mars-like planet, *Icarus,* **211,** 960–985.

Melosh, H.J., 1989. *Impact Cratering: A Geologic Process,* Oxford Monographs on Geology and Geophysics no. 11, Oxford University Press, Oxford.

Melosh, H., 2000. Can impacts induce volcanic eruptions?, http://www.lpl.arizona.edu/~jmelosh/Impact_Volcanism.pdf/.

Ni, S. & Ahrens, T.J., 2006. Surface motion of a fluid planet induced by impacts, *Geophys. J. Int.,* **167,** 1, 445–452.

Nimmo, F., Hart, S.D., Korycansky, D.G. & Agnor, C.B., 2008. Implications of an impact origin of the martian hemispheric dichotomy, *Nature,* **453,** 1220–1223.

Rampino, M.R. & Caldeira, K., 1992. Antipodal hotspot pairs on the Earth, *Geophys. Res. Lett.,* **19,** 20, 2011–2014.

Schultz, P.H. & Gault, D.E., 1974. Seismic effects from major basin formations on the Moon and Mercury, *Earth, Moon Planets,* **12,** 2, 159–177.

Shishkin, N., 2007. Seismic efficiency of a contact explosion and a high-velocity impact, *J. appl. Mech. Tech. Phys.,* **48,** 2, 145–152.

Toon, O.B., Turco, R.P. & Covey, C., 1997. Environmental perturbations caused by the impacts of asteroids and comets, *Rev. Geophys.,* **35,** 1, 41–78.

Wang, Z., Dahlen, F.A. & Tromp, J., 1993. Surface wave caustics, *Geophys. J. Int.,* **114,** 2, 311–324.

Ward, S.N., 2002. Tsunamis, in *Encyclopedia of Physical Science and Technology,* 3rd edn, Vol. 17, pp. 175–191, Elsevier Science, Dordrecht, ISBN 978-0-12-227410-7.

Watts, A.W., Greeley, R. & Melosh, H.J., 1991. The formation of terrains antipodal to major impacts, *Icarus,* **93,** 1, 159–168.

APPENDIX: BENCHMARKS

In this appendix, we briefly discuss a comparison of our results to a hydro-code calculation close to the crater, and two independent benchmarks of our simulations against normal-mode summation in a spherically symmetric earth model using a vertical impact, focusing on the seismic far field.

Ivanov (2005) reports peak displacements of ∼70–80 m and peak velocities of ∼10 $\mathrm{m\,s^{-1}}$ at a crater distance of 300 km in a Chicxulub impact model that was tuned to recreate observed crater features. Ivanov (2005) used an impactor velocity of ∼12 $\mathrm{km\,s^{-1}}$ and diameter of ∼14 km, resulting in a momentum of $\sim 4.6 \times 10^{19}$ N s (larger than in our simulations) and an energy of $\sim 2.8 \times 10^{23}$ J (similar to our simulations). In our approach, at a similar distance, choosing $\tau = 19$ s, we find peak displacements of ∼45 m and peak velocities of ∼10 $\mathrm{m\,s^{-1}}$, whereas for $\tau = 58$ s we obtain peak displacements of ∼10 m and peak velocities of ∼0.7 $\mathrm{m\,s^{-1}}$. While our results and those of Ivanov (2005) are of the same order of magnitude in the first case, they are significantly smaller in the second case, even accounting for the smaller impact momentum used in our simulations. This may be attributed to the dominance of higher frequency waves close to the source, confirming the need for an accurate radiation spectrum close to the impact. In the far field, on the other hand, details of the source spectrum are less important.

Fig. A1 shows vertical surface displacement as a function of time at the antipode as simulated by SPECFEM3D_GLOBE and normal-mode summation using a point source with a value of $\tau = 178$ s and magnitude $F = 3 \times 10^{19}$ N s. The two results are almost indistinguishable. For earthquakes,

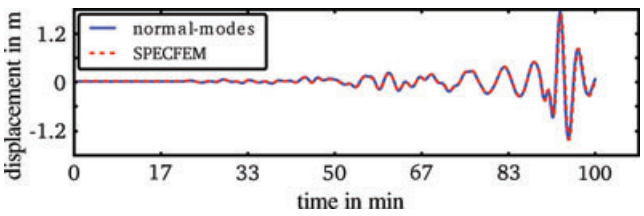

Figure A1. Comparison of vertical-component normal-mode and SEM synthetic seismograms recorded at the antipode due to a vertical point force in spherically symmetric model PREM.

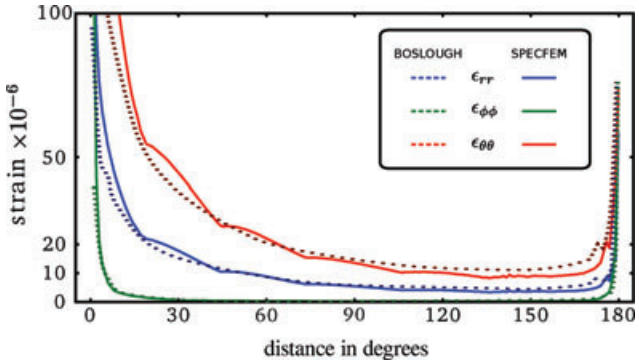

Figure A2. Peak strain after a vertical impact of momentum of 3×10^{19} N s calculated with SPECFEM3D_GLOBE for PREM and by normal-mode summation (by Boslough *et al.* 1996) for model 1066A. The spectral-element calculation uses a Gaussian source–time function with $\tau \sim 48$ s. The modes have periods greater than ∼45 s. The 'scalloping' in the spectral-element calculation is due to sharp upper-mantle discontinuities in PREM, which are largely absent in 1066A.

rather than point forces, SPECFEM3D_GLOBE was extensively benchmarked by Komatitsch & Tromp (2002a). The purpose of this benchmark is to validate the equivalent single-force point-source implementation.

Fig. A2 shows a comparison between our SEM calculations and normal-mode summation for peak strain values along a great circle. The mode calculation was performed by Boslough *et al.* (1996) using modes with periods ≥45 s and a vertical point force. The total transferred momentum is $\Delta p = 3 \times 10^{19}$ N s. Modes were calculated for model 1066A (Gilbert & Dziewonski 1975, including attenuation), and we obtain comparable results for a point source with a value of $\tau = 31$ s. Since we use a different model and source–time function, small deviations are expected, and this figure shows general agreement. We already see that dramatic focusing effects at the antipode lead to peak antipodal strains comparable to regions close to the source. From Fig. A2, it is clear that the region of intense focusing is small. Earth's ellipticity and lateral heterogeneity 'blur' the focusing spot, thereby significantly reducing peak displacement and strains, as discussed in the main body of this paper.